R. L. Satcher, Jr.

S. R. Bussolari

Fluid Mechanics Laboratory,
Department of Mechanical Engineering,
M.I.T.,
Cambridge, MA 02130

M. A. Gimbrone, Jr.

Vascular Research Division,
Department of Pathology,
Brigham and Women's Hospital and
Harvard Medical School,
Boston, MA 02115

C. F. Dewey, Jr.

Fluid Mechanics Laboratory,
Department of Mechanical Engineering,
M.I.T.,
Cambridge, MA 02130

The Distribution of Fluid Forces on Model Arterial Endothelium Using Computational Fluid Dynamics

Numerical calculations are used in conjunction with linear perturbation theory to analyze the problem of laminar flow of an incompressible fluid over a wavy surface which approximates a monolayer of vascular endothelial cells. These calculations model flow conditions in an artery very near the vessel wall at any instant in time, providing a description of the velocity field with detail that would be difficult to identify experimentally. The surface pressure and shear stress distributions are qualitatively similar for linear theory and numerical computations. However, the results diverge as the amplitude of surface undulation is increased. The shear stress gradient along the cell model surface is reduced for geometries which correspond to aligned endothelial cells (versus nonaligned geometries).

I Introduction

The vascular endothelium is the simple epithelium that lines the cardiovascular system. It consists of a cellular monolayer which rests on a complicated matrix of cells and intercellular material. Intact endothelium provides a selectively permeable barrier to the passage of macromolecules from the bloodspace to the extravascular space. Moreover, the vascular endothelium bears the shear stress imparted by blood flow. The structure and function of the monolayer is affected by these mechanical factors (see Fig. 1) [6, 7, 9, 10, 15, 18, 25, 33, 34, 36-39]; however, the specific mechanisms mediating these cellular responses have not been identified.

A detailed description of the flow is needed. An endothelial cell in vivo witnesses flow which passes in rhythmic waves. The cells are only 1-2 μm thick and 20-50 μm in the circumferential and axial dimensions. They are primarily affected by detailed flow behavior very near the wall. In this region, the fluid velocity profile is nearly linear, although the magnitude of the average velocity may vary by a factor of four or more from systole to diastole, and from point to point on the microscopically rough surface. Because of the small size of endothelial cells, flow at any instant may be considered quasi-steady near the wall, as described by the local linear shear flow.

One of the most difficult problems in fluid mechanics is studying flow details near a rough surface. The disturbed wall region is typically buried inside a boundary layer or is difficult to access in experiments. Additional complications include:

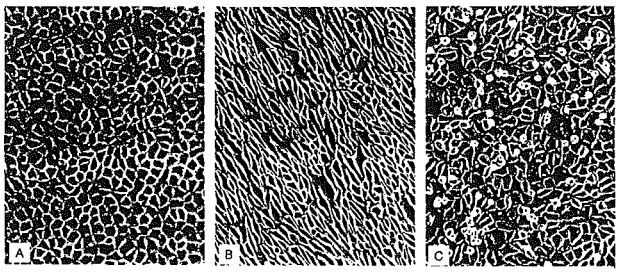

[Davies et al, PNAS 83:2114, 1986]

Fig. 1 Response of vascular endothelium to fluid flow

tiny dimensions (typically microns), wall probe interference effects, and the intrinsic difficulty of accurately measuring wall shear stress. Previous studies demonstrate that numerical solutions of the Navier-Stokes equations yield accurate predictions of flow characteristics in such circumstances [5, 8, 12, 13, 20, 26, 28]. We are using computational methods to study flow near arterial endothelium, whose surface is modelled as a wavy wall.

Endothelial cells withstand fluid forces and maintain intercellular connections in a confluent layer which is only one cell thick in arteries and veins. Preserving the integrity of intercellular junctions is critical for the monolayer to serve its function as a selectively permeable barrier between blood and tissue [6, 25, 38]. When a quiescent monolayer of cells is exposed to flow, the cells can potentially align and elongate in the flow

Contributed by the Bioengineering Division for publication in the JOURNAL OF BIOMECHANICAL ENGINEERING. Manuscript received by the Bioengineering Division November 8, 1991; revised manuscript received February 28, 1992. Associate Technical Editor: M. Friedman.

direction, altering the bulk mechanical characteristics of the cell, and modulating physiological responses in vitro [7, 9, 10, 37, 39]. The nature of this response depends on whether the flow is laminar, disturbed, or turbulent (see Fig. 1). Exposure to shearing forces also causes dramatic changes in the cytoskeleton. The actin network is rearranged from circumferential fibers to form prominent stress fibers [30, 37, 39]. Stress fibers are normally found in the basal aspect of cells which have not experienced shear stress. In such cells, they are arranged in random directions and appear to interconnect regions of adherence of the plasma membrane to the substrate (focal contacts). In aligned cells, stress fibers are parallel to the direction of flow; and appear to attach to the apical membrane [16, 34]. These stress fibers may prevent endothelium from hydrodynamic injury and/or detachment by tethering the apical membrane and stabilizing intercellular junctions. Others have made observations which support this possibility:

- aligned cells appear to be "stiffer" than nonaligned cells as determined by micropipette aspiration [24, 33].
- there is increased ATP utilization in cells exposed to shear stress, presumably in part due to contracting stress fibers [34].
- the permeability of a monolayer with no previous exposure to shear stress is transiently and acutely increased in response to flow [7, 25].

DNA synthesis is altered in cells by exposure to flow affecting gene expression, and apparently producing a different phenotype. Few (if any) other cells in the body experience shearing forces of similar magnitude on only one side. Thus, it is difficult to identify analogous cellular models for comparison. An unrelated phenotypic modulation has been observed in microvessel endothelial cells in response to chemical factors [27]. Similar transdifferentiation studies suggest that extracellular environment, the cytoplasm, and nucleus, interact to confer the gene expression exhibited by cells [23, 27].

In order to understand how shear stress produces such profound effects in endothelial cells, the detailed distribution of forces on a cell and monolayer of cells must first be known. In early studies, investigators did not consider cell shape. The average shearing force imparted by bulk fluid flow was considered determinant: high shear stress caused direct desquamation, and low shear stress caused concentration polarization effects at the wall [6, 14]. Subsequent studies suggest that disturbed flow patterns (such as are found near branchings in arteries) are more closely associated with possible pathological processes [15]. The flow field in such regions is characterized by high shear stress gradients. Theoretical and experimental work has demonstrated the importance of local geometry, corresponding to cell shape in our problem, in affecting the flow field near a surface [6, 15]. In cases where the surface geometry scaling is much smaller than bulk flow conduit geometry, the stress distribution depends on the local flow field induced by the object [4, 22]. For a wavy surface, the relevant flow field is contained in a small region near the wall that scales with the wavelength of the surface variation.

The wavy wall problem has been studied in two dimensions by others [2, 5, 20, 22, 26, 28]. Such computations were used for studying wave growth under the influence of wind (beach processes). Theoretical solutions for steady flows at large hydraulic Reynold's number (Re) over small-amplitude wavy surfaces were obtained [2, 5, 26]. Similar calculations have been performed for low Re oscillatory flows over wavy surfaces [20, 22, 28]. The theory for our problem follows from these latter works.

Recent studies include numerical treatments of low Re flows over objects in shear flows. In one study, finite elements are used to estimate forces acting on a thrombus [13]. We apply linear theory to predict the local flow field over a coordinate surface which models an endothelial cell monolayer (see Appendix) [4]. A comparison is made with results from spectral element numerical calculations in order to define the range of geometric parameters for which linear theory is applicable.

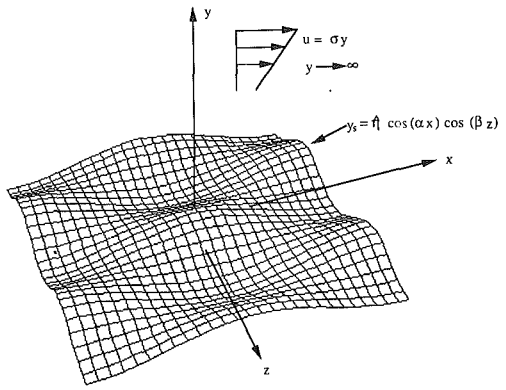

Fig. 2 Cell surface model

II Computational Methods

A model surface was chosen which represents the cell monolayer (see Fig. 2). The fluid flow near this surface is characterized by a vanishing Reynold's number [$\mathrm{Re} \sim O(10^{-4})$] so that momentum transfer is dominated by viscous forces. The pertinent governing equations are for an incompressible, constant-property, steady-state fluid, leading to a so-called Stokes calculation. Conservation of momentum and mass can be written as (respectively):

$$\frac{1}{\mathrm{Re}} \nabla^2 \bar{u} = \nabla p \tag{1}$$

$$\nabla \bar{u} = 0 \tag{2}$$

The unknowns are the vector velocity $\bar{u}$ and the pressure p. The single parameter appearing is the Reynold's number, $\mathrm{Re} = \sigma \hat{\eta}^2 / \nu$, where σ is the shear rate in the linear shear flow far from the surface, and $\hat{\eta}$ is the surface undulation amplitude (characteristic length scale of the problem). The kinematic viscosity of the fluid is $\nu \equiv \mu/\rho$, where ρ is the fluid density and μ is the fluid viscosity. The equations are parabolic so velocity boundary conditions must be provided on all sides of the computational domain. The complete theoretical solution is included in the Appendix [4].

Our calculations simulate conditions in large arteries (such as the aorta) very near the vessel wall at any instant in time. The upper boundary can be represented as a shear flow at infinite distance from the surface. However, the computational code did not explicitly provide for boundary conditions at infinity. Instead we specified the upper boundary to be a rigid surface which is moved far enough away (at least 4 times the cell surface modulation amplitude) so that wall effects are no longer important. The velocity at the upper surface is fixed at the value corresponding to a linear shear flow field. The cell surface is the lower boundary of the domain. It is rigid and extends infinitely in x and z. Thus, the solution is determined by solving for one full period of the cell model surface in the relevant directions (x and z). Boundary conditions are expressed below:

$$|\bar{u}|_{y \to \infty} = \sigma y \text{ (shear flow at large distance)}$$

$$|\bar{u}|_{y = y_s} = 0 \text{ (zero velocity at wall)}$$

where σ is the undisturbed shear rate far away from the wall. A shear rate of $\sigma = 800\ \mathrm{s}^{-1}$ was specified for all calculations. Unsteady motion dynamics for physiologic frequencies are such that a quasi-steady approximation can be made ($\alpha = h\sqrt{\omega/\nu} = 0.1$ to 0.001).

The computational code NEKTON was used for numerical solution of the problem [12, 29, 31]. This code is robust and efficient, and was easily modified to generate the model cell

surface as the lower boundary of the computational domain. NEKTON has powerful pre- and post-processing packages for mesh generation and visualization of results. The code runs on a wide variety of computers (from workstations to supercomputers). Thus, computational experiments can be performed on smaller machines, while production runs can be directed to the most efficient computers available [8, 11]. Only three-dimensional steady-state Stokes results are presented in this paper (quasi-steady approximation), although NEKTON supports both unsteady and three-dimensional incompressible fluid calculations for the full Navier-Stokes equations.

The spectral element method for partial differential equations is the basis for spatial discretization. The method is summarized briefly in what follows. For an extensive description, one should see references 29 and 31. Spectral elements combine high-order (spectral) accuracy with the geometrical flexibility of low order finite-element methods. The computational domain is divided into K nondegenerate macro-quadrangles (spectral elements). In our problem, three-dimensional domains were broken up into "bricks," in which the two horizontal parallel faces are nondegenerate quadrangles [8, 11, 29].

The data, geometry, and solution, are approximated by high order polynomial expansions within each macro-element. A local Cartesian mesh is constructed within each element which corresponds to $N \times N \times N$ tensor-product Gauss-Lobatto Legendre collocation points. The Gauss-Lobatto points are clustered near elemental boundaries; an arrangement which gives accurate approximation, and favorable interpolation and quadrature properties. Dependent variables are expanded in terms of $(N-1)^{\text{th}}$ order polynomial Lagrangian interpolants (through the Gauss-Lobatto Legendre collocation points) [8, 11, 12].

Spatially discrete equations are generated by inserting assumed forms of dependent variables into the governing equations, and requiring that the residual vanish in some integral and weighted sense. The computed numerical variables correspond to values occurring at the collocation points of the mesh. Convergence is obtained by increasing the number of macro-elements (K) or the order of the interpolants (N) in the elements. The error decreases algebraically (like K^{-N}) as K is increased; and exponentially for smooth solutions (like $e^{-\alpha N}$) as N is increased [8, 11].

For our computations, two domains in x and z, and one in y (total of 4) were adequate to resolve the details of the flow. Increased accuracy (in the spectral sense) was achieved by increasing the polynomial degree. The present calculations used values of N between 7 and 11. Calculations were performed on a Concurrent 6450 computer.

III Results

An analytical solution for linearized flow over a wavy wall is given in the Appendix [4]. The amplitude of the sinusoidal boundary modulation must be small relative to the wavelength. If this condition is satisfied, the boundary condition at the cell model surface, y_s, can be linearized. The function which defines the surface is:

$$y_s = \hat{\eta}\cos(\alpha x)\cos(\beta z) \tag{3}$$

where $\hat{\eta}$ is the amplitude of surface oscillation. The streamwise and transverse wavenumbers α and β are given by,

$$\alpha = \frac{2\pi}{\lambda_x};\ \beta = \frac{2\pi}{\lambda_z} \tag{4}$$

where λ_x and λ_z are the surface undulation wavelengths. The resulting dimensionless shear stress and pressure force distributions on the model endothelial surface are:

$$\tau^*_{yx} = 1 + 2\pi\,\frac{2+q^2}{\sqrt{1+q^2}}\,\frac{\hat{\eta}}{\lambda_x}\cos(\alpha x)\cos(\beta z) \tag{5}$$

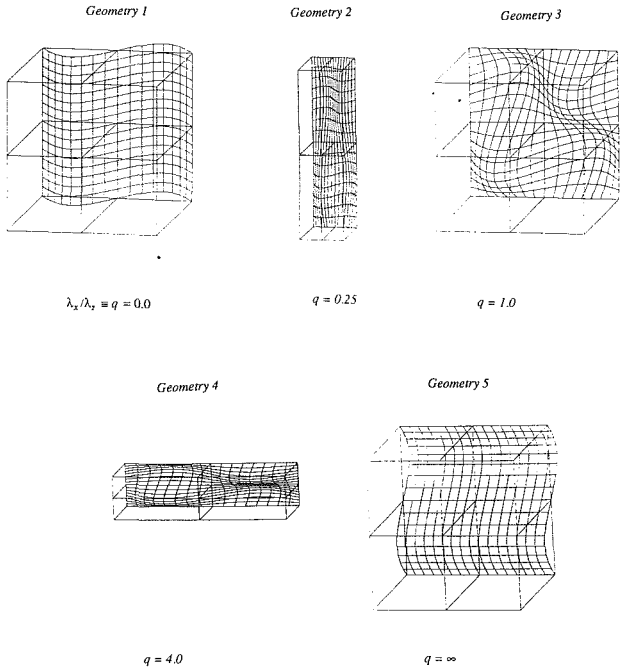

Fig. 3 Surface geometries defined by a length (λ_x) and width (λ_z) of undulation

$$\tau^*_{yz} = -2\pi\,\frac{q}{\sqrt{1+q^2}}\,\frac{\hat{\eta}}{\lambda_x}\sin(\alpha x)\sin(\beta z) \tag{6}$$

$$p^* = -4\pi\,\frac{\hat{\eta}}{\lambda_x}\sin(\alpha x)\cos(\beta z) \tag{7}$$

where,

$$q = \frac{\lambda_x}{\lambda_z} = \frac{\beta}{\alpha} = \frac{\text{length}}{\text{width}} \tag{8}$$

$$\tau^*_{yx} = \frac{\tau_{yx}}{\mu\sigma},\ \tau^*_{yz} = \frac{\tau_{yz}}{\mu\sigma};\ p^* = \frac{p}{\mu\sigma} \tag{9}$$

τ^*_{yx} is the normalized surface shear stress in the x-direction; and τ^*_{yz} is the normalized surface shear stress in the z-direction. The term $\mu\sigma$ is the mean wall shear stress imposed by flow far (i.e., many times the cell height) from the endothelial surface. The solution predicts:

1. The surface shear stress in the x-direction consists of the sum of the average shear stress imposed by flow and a spatially varying stress perturbation due to cell shape. The magnitude of the shear stress perturbation depends on q and $\hat{\eta}/\lambda_x$. As $\hat{\eta}/\lambda_x$ (dimensionless surface amplitude) increases, the perturbation increases linearly. For $q \gg 1$ it is proportional to q. τ^*_{yx} is in phase with surface variations in x and z—it is maximum at the highest point on the cell surface, and minimum at the lowest point on the surface.

2. The presence of surface waviness introduces a lateral shear stress perturbation which is linear with $\hat{\eta}/\lambda_x$. It is caused by the transverse flow away from surface peaks and toward surface valleys. As q becomes large ($\gg 1$), there is no dependence on q. τ^*_{yz} is $\pi/2$ out of phase with the surface waviness in the streamwise and transverse directions. It is maximum or minimum at points of maximum surface slope.

3. The pressure perturbation is linear with $\hat{\eta}/\lambda_x$, but does not depend on q. It is asymmetric along the cell longitudinal axis, tending to increase the pressure on the proximal side and reduce it on the distal side. The pressure is $\pi/2$ out of phase with the surface variations in the direction of flow. Pressure is maximum or minimum at points of maximum slope in the flow direction.

Numerical and analytical computations were compared for

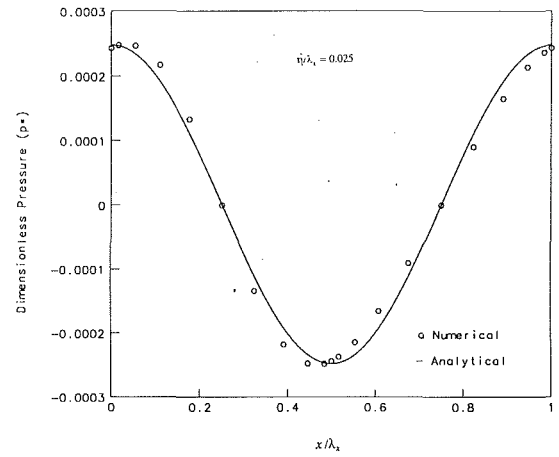

Fig. 4(*a*)

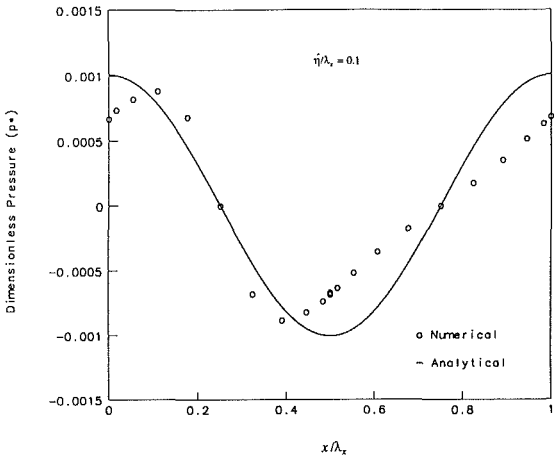

Fig. 4(*b*)

Fig. 4 Surface pressure distribution profiles for the case of $q = 1$

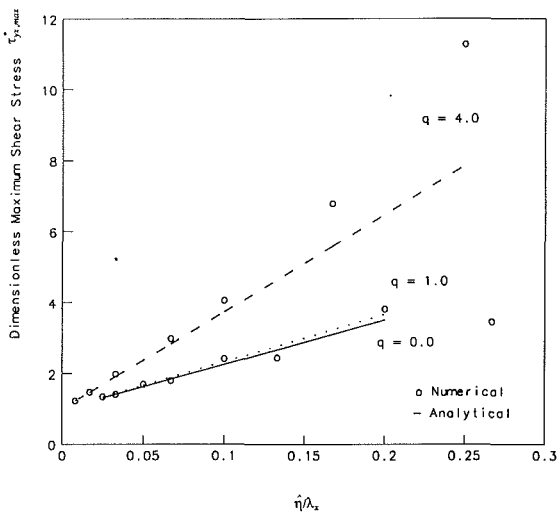

Fig. 5(*a*)

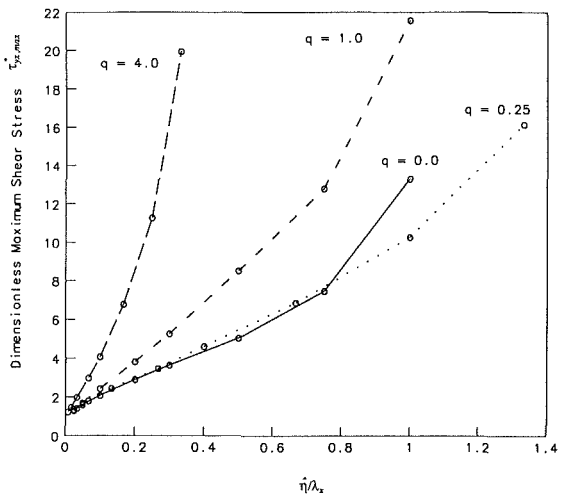

Fig. 5(*b*)

Fig. 5 Dimensionless maximum shear stress ($\tau^*_{yx,max}$) vs. height/length for (*a*) numerical and analytical solutions and (*b*) numerical solution

5 surface geometries: length/width ratios of $q = 0$, 0.25, 1, 4, and ∞ (see Fig. 3). Eight amplitudes ($\hat{\eta} = 1$, 2, 4, 8, 12, 20, 30, and 40 μm) were evaluated for each geometry. The resulting range for the height/length ratio [$0 \leq \hat{\eta}/\lambda_x \leq 4/3$] includes values which violate the condition $\hat{\eta}/\lambda_x \ll 1$. Physiologic values of length/width ratio for large vessel endothelial cells typically range from 0.25 to 4.0 [4]. Cell heights (corresponding to surface amplitude) are usually 1–4 μm.

For a limited range, numerical results and linear theory predictions agree (not illustrated). Both numerical and theoretical methods predict that the wall shear stress τ^*_{yx} is maximum at the highest points of the coordinate surface, and minimum at the lowest points. The pressure distribution is $\pi/2$ out of phase in the direction of flow, and the wall shear stress and pressure distributions are periodic.

Numerical *magnitudes* no longer agree with linear theory after the onset of separated flow. Figures 4(*a*) and 4(*b*) compare pressure distribution profiles for $q = 1$ as $\hat{\eta}/\lambda_x$ is increased from 0.025 (Fig. 4(*a*)), to 0.1 (Fig. 4(*b*)) (Note: for plotting purposes, the origin was shifted by 90° so that the peak in the pressure profile occurs at the origin). The linear solution no longer closely follows numerical predictions as the dimensionless surface amplitude becomes of O(0.1), where recirculations appear in the flow field.

Maximum ($\tau^*_{yx,max}$) and minimum ($\tau^*_{yx,min}$) shear stress magnitudes for both numerical and analytical solutions are plotted in Figs. 5(*a*) and 6(*a*) for a range of parameter values. Groups of points corresponding to a particular geometry (fixed length/width value) fall along the same line when shear stress and pressure are plotted vs. surface amplitude (Figs. 5–7). The maximum wall shear predictions are in better agreement than the minimum wall shear values. As shown in Fig. 5(*a*), the maximum wall shear values increase almost linearly for $\hat{\eta}/\lambda_x < 0.2$. The slopes agree initially, but diverge as the amplitude increases. This effect becomes more pronounced for higher q values. Figure 5(*b*) is a plot of the numerical maximum shear stress data. As the dimensionless amplitude is increased well beyond 0.2, nonlinear behavior prevails. For minimum wall shear, the analytical solution predicts a linear decrease with increasing $\hat{\eta}/\lambda_x$ (Fig. 6(*a*)). But for $\hat{\eta}/\lambda_x > 0.1$, the numerical result diverges. This difference is attributable to the formation of regions of reverse flow.

Linear theory fails to predict reverse flow. It only accounts for flow accelerations and decelerations due to expansion or contraction of the flow domain. Describing the relevant processes which cause recirculation would require using higher order terms in the analytical model. The numerical solution predicts and resolves flow reversals as the dimensionless amplitude is increased. As shown in Fig. 8, streamline plots indicate that vortices form in the valleys of the cell model surface. Recirculation regions occur when there is surface variation in the primary flow direction (i.e., for *Geometries 1-4*).

We did not resolve the exact amplitude where recirculation begins; however, the range which contains the critical amplitude is recorded in the table in Fig. 8. The critical dimensionless surface amplitude is of O(0.1), and it defines 2 regions:

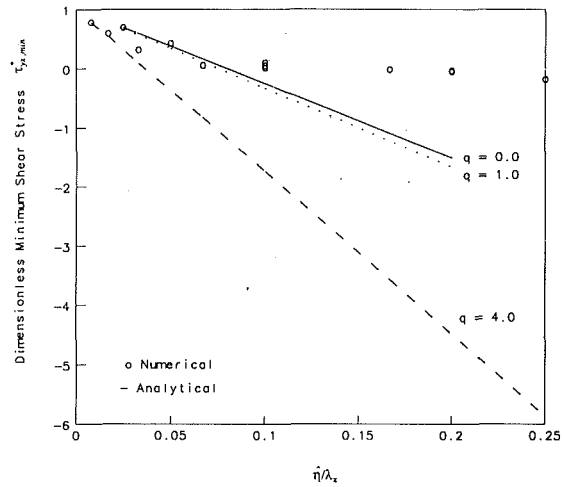

Fig. 6(*a*)

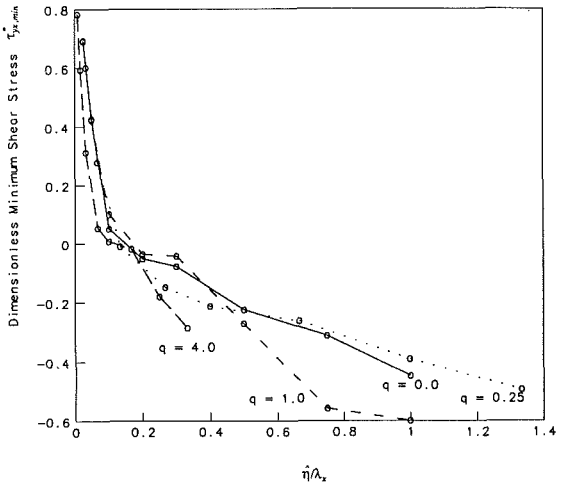

Fig. 6(*b*)

Fig. 6 Dimensionless minimum shear stress ($\tau^*_{yx,min}$) vs. height/length for (*a*) numerical and analytical solutions and (*b*) numerical solution

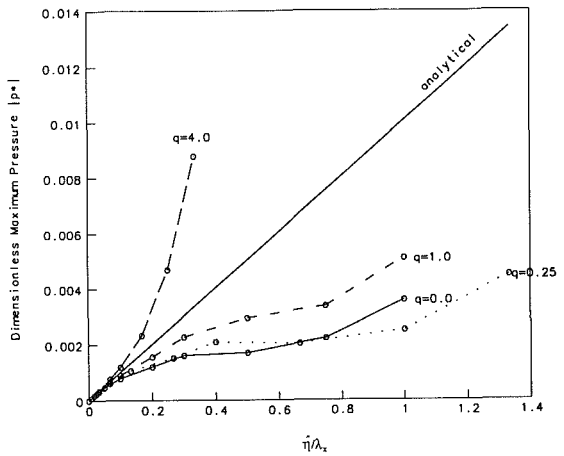

Fig. 7 Dimensionless maximum pressure magnitude ($|p^*|$) vs. height/length for numerical and analytical solutions

1. For $\hat{\eta}/\lambda_x < (\hat{\eta}/\lambda_x)_{crit}$, the numerical values are in good agreement with linear theory.

2. For $\hat{\eta}/\lambda_x > (\hat{\eta}/\lambda_x)_{crit}$, the values diverge. The physical processes can no longer be represented by a linear perturbation. Higher order terms are needed for a more accurate theoretical treatment.

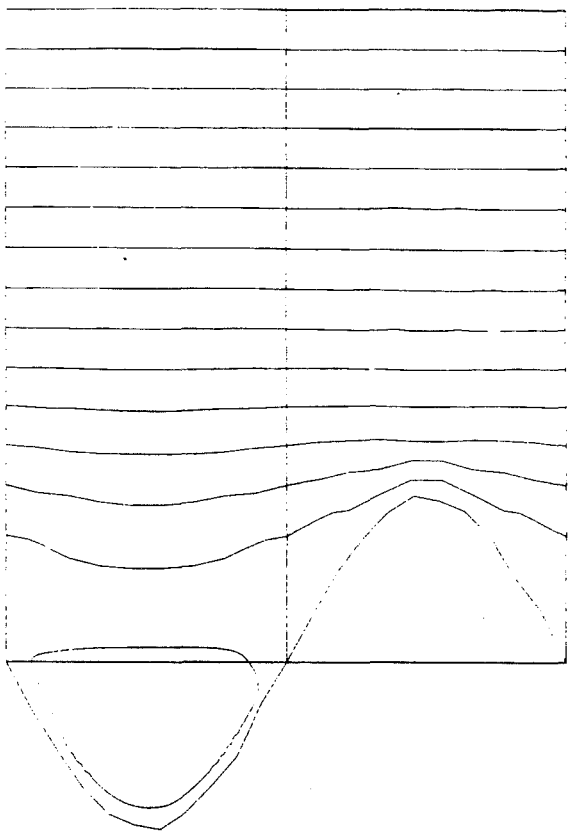

Vortices Appear		
Geometry	Crit. ampl. range	q
Geometry 1	0.10-0.20	0.00*
Geometry 2	0.07-0.13	0.25
Geometry 3	0.10-0.20	1.00
Geometry 4	0.10-0.16	4.00
Geometry 5	**	∞**

*Transverse ribs

**Vortices do not appear: streamwise ribs

Fig. 8 Streamline plot for the case of $q = 1$; $\hat{\eta}/\lambda_x = 0.5$ showing a region of recirculation. Fluid flow is from left to right. The table indicates the value of the dimensionless surface amplitude at which vortices are first observed for each of the geometries.

The analytical solution for surface pressure predicts a linear dependence on $\hat{\eta}/\lambda_x$, and no dependence on q. The numerical result exhibits dependence on q; namely, the slope increases with q (Fig. 7). In contrast, the symmetrical *form* of the numerical solution agrees with linear theory. The average surface pressure must be zero so that there is no net flow in the direction normal to the top boundary. With *Geometry 5*, the pressure field is zero everywhere (for both numerical and analytical results) since there is no surface variation in the flow direction.

IV Discussion

The flow fields predicted by the numerical and analytical solutions are qualitatively similar. The wall shear stress and pressure distributions vary periodically at the wavy wall surface. However, the results from the two methods diverge as the amplitude of the surface waviness increases. Flow vortices appear as the key assumption of linear theory is violated (namely, $\hat{\eta}/\lambda_x \ll 1$—see Appendix), where the critical dimensionless amplitude is of O(0.1). Departure from linear

ear theory predictions can be observed by comparing surface pressure distributions (Figs. 4(*a*) and 4(*b*)). There is:

- a departure from linear growth of peak-to-peak pressure.
- variation in the phase of pressure distribution.
- contributions from higher harmonics of the pressure distribution.
- dependence on the length/width ratio (parameter q).

Others have obtained similar predictions [2, 5, 22]. Linear theory does not predict the formation of recirculation regions, since the physical phenomena responsible for vortex flow are nonlinear processes. Adverse pressure gradients arise in the regions between surface peaks, inducing a reverse flow when the fluid momentum can no longer overcome the pressure gradient. As recirculation regions form in geometries of low aspect ratio (q), the pressure profile predicted by linear theory is relaxed. The momentum of the flow that would be lost in the pressure recovery region (trough) is preserved as the flow separates. In geometries of higher q, the vortices are smaller due to the transport of momentum around the sides of the peaks into the low pressure region and thus the "shadowing effect" of the vortices is reduced. The flow passing over the smaller vortices impinges on the proximal sides of the surface peaks, resulting in higher peak pressures near the points of maximum slope.

At the highest surface points, the wall shear stress grows almost linearly with increasing surface amplitude as predicted by linear theory. Flow acceleration occurs along streamlines toward the peaks due to the constraint provided by the continuity equation. These processes are different than those producing flow separation in the lower surface regions.

Nonuniform shear stress gradients of significant magnitude across a cell surface could be of potential importance for explaining flow induced morphological changes. The forces which result from a cell-to-cell variation on the order of the perturbation shear stress are sufficient to disturb protein-protein interactions. Bell [1] has determined that a noncovalent interaction is disrupted by a critical force of 10^{-5} dyne. The difference in shear force on 2 adjacent cells in laminar flow can be of order 10^{-4} dyne, which corresponds to 10 protein-protein interactions. Experimental studies of others indicate that a force of ~ 1 dyne (10^5 protein-protein interactions) can detach a cell from a monolayer [21]. Thus, the imbalance forces produced by surface variations are potentially large enough to disturb small numbers of a cell's protein-protein noncovalent associations with other cells, but cannot detach the cells. An endothelial monolayer will have more geometric variability than our model; consequently, the resulting shear stress gradients could exceed those predicted for the model surface. A sequential disruption of a large number of bonds holding a monolayer together could lead to alterations in cell morphology.

The predicted forces acting on the aligned monolayer are reduced in comparison to nonaligned endothelium. For a surface approximating a nonaligned monolayer, the perturbation shear stress can be as large as 34 percent of the average shear stress imposed by the primary flow. This decreases to 20 percent for aligned monolayers since the height/length ratio is reduced (essentially, the surface is less "bumpy"). Perhaps the monolayer is able to achieve stability by reconfiguring the actin filament system so that stress fibers attach to the apical membrane. Nonaligned cells do not have stress fibers in the proper arrangement to experience this stabilizing effect.

Modeling the distribution of forces on cells also aids in understanding the role of shear stress in the pathophysiology of atherosclerosis. Endothelium exposed to large shear stress *gradients* displays dramatic changes in cell shape, density, and rate of division [9, 15]. Our analysis predicts that shear stress gradients associated with laminar flow are smaller in magnitude than disturbed or turbulent flow. Consequently, the observed endothelial response to laminar flow is marked (cells elongate in the flow direction), but differs from disturbed flow in that there is little change in cell division and density [7, 9, 10]. Loss of contact with neighboring cells has been shown to induce migration and cell shape changes [7, 37]. Thus the larger forces associated with disturbed flow may exceed the cells' adaptive capabilities, resulting in pathological behavior. Observed responses include: increased cell division, changes in cell density, altered arachidonate metabolism, growth factor and cytokine production, surface adhesive properties, coagulation and fibrinolytic activities and altered permeability to macromolecules and lipoproteins [17–19].

Acknowledgments

We thank Prof. A. T. Patera of M.I.T. and Dr. Einar Ronquist of Nektonics for assistance with the computational program.

References

1 Bell, G. I., "Models for the Specific Adhesion of Cells to Cells," *Science*, Vol. 200, 1978, p. 618.

2 Benjamin, T. B., "Shearing Flow Over a Wavy Boundary," *J. of Fluid Mechanics*, Vol. 6, 1959, pp. 161–205.

3 Bussolari, S. R., Dewey, C. F. Jr., and Gimbrone, M. A. Jr., "Apparatus for Subjecting Living Cells to Fluid Shear Stress," *Rev. Sci. Instruments*, Vol. 53, No. 12, 1982, pp. 1851–1854.

4 This unpublished work appeared in Bussolari, S. R., "The Dynamic Response of Vascular Endothelium to Fluid Shear Stress in Vitro," Ph.D. thesis, MIT, 1983.

5 Caponi, E. A., Fornberg, B., Knight, D. D., McLean, J. W., Saffman, P. G., and Yuen, H. C., "Calculations of Laminar Viscous Flow over a Moving Wavy Surface," *J. of Fluid Mechanics*, Vol. 124, 1982, pp. 347–362.

6 Caro, C. G., Fitz-Gerald, J. M., and Schroter, R. C., "Atheroma and Arterial Wall Shear. Observation, Correlation and Proposal of a Shear-Dependent Mass Transfer Mechanism for Atherogenesis," *Proc. R. Soc. Lond. B Biol. Sci.*, Vol. 365, 1985, p. 92.

7 Davies, P. F., Remuzzi, A., Gordon, E. J., Dewey, C. F. Jr., and Gimbrone, M. A. Jr., "Turbulent Fluid Shear Stress Induces Vascular Endothelial Cell Turnover In Vitro," *Proc. Natl. Acad. Sci.*, Vol. 83, 1986, pp. 2114–2117.

8 DePaola, N., Ronquist, E. M., and Dewey, C. F. Jr., "Wall Shear Stresses Produced by Surface Protuberances in a Linear Shear Flow," International Conference on Spectral and High Order Methods for Partial Differential Equations," ICOSAHAM, 1989, Como, Italy.

9 DePaola, N., Gimbrone, M. A., Jr., Davies, P. F., and Dewey, C. F., Jr., "Vascular Endothelium Responds to Fluid Shear Stress Gradients," *Arteriosclerosis and Thrombosis*, 1992 (in press).

10 Dewey, C. F. Jr., Bussolari, S. R., Gimbrone, M. A. Jr., and Davies, P. F., "The Dynamics Response of Vascular Endothelial Cells to Fluid Shear Stress," ASME JOURNAL OF BIOMECHANICAL ENGINEERING, Vol. 103, 1981, p. 177.

11 Dewey, C. F. Jr., and DePaola, N., "Exploring Flow-Cell Interactions Using Computational Fluid Dynamics," ASME/JSME Tissue Engineering Symposium, ASME Winter Annual Meeting, 1989, San Francisco.

12 Fischer, P. F., and Patera, A. T., "Parallel Spectral Element Solution of the Stokes Problem," *J. Comput. Phys.*, Vol. 92(2), 1991, pp. 380–421.

13 Folie, B. J., and McIntire, L. V., "Mathematical Analysis of Mural Thrombogenesis," *Biophysical Journal*, Vol. 56, 1989, pp. 1121–1141.

14 Fox, J. A., and Hugh, A. E., "Localization of Atheroma: A Theory Based on Boundary Layer Separation," *British Heart Journal*, Vol. 28, 1966, pp. 388–399.

15 Fry, D. L., "Acute Vascular Endothelial Changes Associated with Increased Blood Velocity Gradients," *Circulation Research*, Vol. 22, 1968, pp. 165–197.

16 Personal communication: Gimbrone, M. A. Jr.

17 Gimbrone, M. A. Jr., "Endothelial Dysfunction and Atherosclerosis," *J. Cardiac Surgery*, Vol. 4(2), 1989, pp. 180–183.

18 Gimbrone, M. A. Jr., "Endothelial Dysfunction and the Pathogenesis of Atherosclerosis," Fidge, N. H., Nestel, P. J., eds., *Atherserlerosis VII, Proc. 7th Intl. Symp. on Atherosclerosis, Amsterdam, Excerpta Medica*, 1986, pp. 367–369.

19 Gimbrone, M. A. Jr., Bevilacqua, M. P., and Cybulsky, M. I., "Endothelial-Dependent Mechanisms of Leukocyte Adhesion in Inflammation and Atherosclerosis," *Annals NY Acad. Sci.*, 598, 1990, pp. 77–85.

20 Hara, T., and Mei, C. C., "Oscillating Flows Over Periodic Ripples," *J. of Fluid Mechanics*, Vol. 211, 1990, pp. 183–209.

21 Hubbe, M. A., "Adhesion and Detachment of Biological Cells In Vitro," *Progress in Surface Science*, Vol. 11, 1981, p. 65.

22 Hyman, W. A., "Shear Flow Over a Protrusion From a Plane Wall," *J. Biomechanics*, Vol. 5, 1972, pp. 45–48.

23 Ingber, D. E., "Fibronectin Controls Capillary Endothelial Cell Growth by Modulating Cell Shape," *Proc. Natl. Acad. Sci.*, (1990) Vol. 87: pp. 3579–3583.

24 Janmey, P. A., Euteneuer, U., Traub, P., Schliwa, M., "Viscoelastic Properties of Vimentin Compared with Other Filamentous Biopolymer Networks," *Journal of Cell Biology*, Vol. 113(1), 1991, pp. 155–160.
25 Jo, H., Dull, R. O., Hollis, T. M., and Tarbell, J. M., "Endothelial Albumin Permeability is Shear Dependent, Time Dependent, and Reversible," *Am. J. Physiology, Heart & Circulation Physiology*, 1991, 260, pp. H1992–H1996.
26 Kiya, M., and Arie, M., "Viscous Shear Flow Past Small Bluff Bodies Attached to a Plane Wall," *J. of Fluid Mechanics*, Vol. 69, 1975, pp. 803–823.
27 Lipton, B. H., Bensch, K. G., and Karasek, M. A., "Microvessel Endothelial Cell Transdifferentiation: Phenotypic Characterization," *Differentiation*, Vol. 46, 1991, pp. 117–133.
28 Lyne, W. H., "Unsteady Viscous Flow Over a Wavy Wall," *J. of Fluid Mechanics*, Vol. 50(1), 1971, pp. 33–48.
29 Maday, Y., and Patera, A. T., "Spectral Element Methods for the Incompressible Navier-Stokes Equations," State of the Art Surveys on Computational Mechanics, eds., Noor, A. K., Oden, J. T., 1989, pp. 71–143.
30 Matsudaira, P., "Modular Organization of Actin Crosslinking Proteins," *TIBS*, Vol. 16, 1991, pp. 87–92.
31 Ronquist, E. M., and Patera, A. T., "Spectral Element Multigrid. I. Formulation and Numerical Results," *J. Sci. Comput.*, Vol. 2(4), 1987, pp. 389–406.
32 Sachs, F., *Cell Shape: Determinants, Regulation and Regulatory Role*, eds.: Stein, W. D., Bronner, F., Academic, San Diego, CA, 1989, pp. 63–92.
33 Sato, M., Levesque, M. J., and Nerem, R. M., "Micropipette Aspiration of Cultured Bovine Aortic Endothelial Cells Exposed to Shear Stress," *Arteriosclerosis*, Vol. 7(3), 1916, pp. 276–286.
34 Schnittler, H., Franke, R. P., and Drenckhahn, D., "Role of the Endothelial Actin Filament Cytoskeleton in Rheology and Permeability," *Z. Kardiologie*, Suppl. 78(6), 1989, pp. 1–4.
35 Sdougos, H. P., Bussolari, S. R., and Dewey, C. F. Jr., "Secondary Flow and Turbulence in a Cone-and-Plate Device," *J. of Fluid Mechanics*, Vol. 138, 1984, pp. 379–404.
36 Shen, J., Luscinskas, F. W., Gimbrone, M. A. Jr., and Dewey, C. F. Jr., "Flow Modulates Cytosolic Calcium Response of Vascular Endothelial Cells to Adenine Nucleotides," submitted 1991.
37 Wechezak, A. R., Wight, T. N., Viggers, R. F., and Sauvage, L. R., "Endothelial Adherence under Shear Stress is Dependent Upon Microfilament Reorganization," *Journal of Cell Physiology*, Vol. 139, 1989, pp. 136–149.
38 Weinbaum, S., Tzehgai, G., Ganatos, P., Pfeffer, R., and Chien, S., "Effect of Cell Turnover and Leaky Junctions on Arterial Macromolecular Transport," *Am. J. Physiology, Heart & Circulation Physiology*, Vol. 248, 1985, pp. H945–H960.
39 White, G. E., Gimbrone, M. A. Jr., and Fujiwara, K., "Factors Influencing the Expression of Stress Fibers in Vascular Endothelial Cells In Situ," *Journal of Cell Biology*, Vol. 97, 1983, p. 416.

APPENDIX

Linear Flow Over a Wavy Wall

The governing Navier-Stokes equations and boundary conditions are given in Eqs. (1) and (2), and two paragraphs following them. For the Reynolds number Re approaching zero, the equations reduce to those of Stokes with boundary conditions appropriate to linear shear flow:

$$\frac{\partial u}{\partial x}+\frac{\partial v}{\partial y}+\frac{\partial w}{\partial z}=0 \tag{A-1}$$

$$\frac{\partial^2 u}{\partial x^2}+\frac{\partial^2 u}{\partial y^2}+\frac{\partial^2 u}{\partial z^2}=\frac{1}{\mu}\frac{\partial P}{\partial x} \tag{A-2}$$

$$\frac{\partial^2 v}{\partial x^2}+\frac{\partial^2 v}{\partial y^2}+\frac{\partial^2 v}{\partial z^2}=\frac{1}{\mu}\frac{\partial P}{\partial y} \tag{A-3}$$

$$\frac{\partial^2 w}{\partial x^2}+\frac{\partial^2 w}{\partial y^2}+\frac{\partial^2 w}{\partial z^2}=\frac{1}{\mu}\frac{\partial P}{\partial z} \tag{A-4}$$

$$\text{for } y\to\infty,\ u=\sigma y, \text{ and } (v,\ w)=0 \tag{A-5}$$

where σ is the shear rate. The boundary condition at the surface requires $(u,\ v,\ w)$ to vanish.

A linearized solution is sought: that is, the velocity field is described by the solution to the problem of linear shear flow over a flat wall (Couette flow) plus a small perturbation caused by wall waviness. The velocity perturbation must vanish at infinity, recovering Eq. (A-5), and the sum of the velocity perturbations and the linear shear flow must be zero at the perturbed wall surface.

Linearization of the Equations. The wavy wall can be expressed in analytical form by the equation:

$$y=\eta\equiv\hat{\eta}e^{i(\alpha x+\beta z)} \tag{A-6}$$

Only the real part of Eq. (A-6) is taken to have physical significance. Equation (A-6) defines a surface with waviness in both the x and z directions with amplitude $\hat{\eta}$ and wavenumbers α and β, respectively. To facilitate manipulation of the equations, the symbol η will be used to indicate the surface, implying the right-hand side of Eq. (A-6).

The form assumed for the velocities and pressure is as follows:

$$u=U+\hat{u}(y)e^{i(\alpha x+\beta z)} \tag{A-7}$$

$$v=\hat{v}(y)e^{i(\alpha x+\beta z)} \tag{A-8}$$

$$w=\hat{w}(y)e^{i(\alpha x+\beta z)} \tag{A-9}$$

$$P=\hat{P}(y)e^{i(\alpha x+\beta z)} \tag{A-10}$$

$U=\sigma y$ is the Couette flow solution. The form of the pressure and velocity perturbations are the product of: 1) an unknown function of y alone; and 2) a periodic function of x and z that matches the form of the boundary η. The boundary conditions on the velocities are:

at the surface, $y=\eta$:

$$\hat{u}(\eta)+\sigma\eta=0 \tag{A-11}$$

$$\hat{v}(\eta)=0 \tag{A-12}$$

$$\hat{w}(\eta)=0 \tag{A-13}$$

and, for $y\to\infty$:

$$\hat{u}(\infty)=\hat{w}(\infty)=\hat{v}(\infty)=0 \tag{A-14}$$

$$\hat{u}'(\infty)=\hat{v}'(\infty)=\hat{w}'(\infty)=0 \tag{A-15}$$

where primes denote differentiation with respect to y.

When the velocities and pressure given by Eqs. (A-7)–(A-11) are substituted in Eqs. (A-1)–(A-4), the following results:

$$i\alpha\hat{u}+\hat{v}'+i\beta\hat{w}=0 \tag{A-16}$$

$$\hat{u}''-K^2\hat{u}=\frac{1}{\mu}i\alpha\hat{P} \tag{A-17}$$

$$\hat{v}''-K^2\hat{v}=\frac{1}{\mu}i\alpha\hat{P}' \tag{A-18}$$

$$\hat{w}''-K^2\hat{w}=\frac{1}{\mu}i\beta\hat{P} \tag{A-19}$$

where

$$K^2=\alpha^2+\beta^2 \tag{A-20}$$

By some algebraic manipulation, Eqs. (A-16) through (A-19) can be combined to produce the following single fourth-order differential equation in terms of K:

$$\hat{v}''-K^2\hat{v}=\frac{1}{K^2}(\hat{v}''''-K^2\hat{v}'') \tag{A-21}$$

Linearization of the Boundary Conditions. If the amplitude of the waviness $\hat{\eta}$ is small and the wavelengths in both the x and z directions are long, the lower boundary condition can be linearized to the following form:

$$\hat{u}(0)=-\sigma\hat{\eta};\ \hat{v}(0)=\hat{w}(0)=0 \tag{A-22}$$

The form of the continuity equation (Eq. A-16) provides a second constraint on $\hat{v}$ at $y=0$:

$$\hat{v}'(0)=i\alpha\hat{\eta}\sigma \tag{A-23}$$

Transformation of Variables. It is convenient to transform to a new variable ψ:

$$\psi=\hat{v}''-K^2\hat{v} \tag{A-24}$$

The transformed form of Eq. (A-21) is

$$\psi''-K^2\psi=0 \tag{A-25}$$

which has a general solution

$$\psi = Ae^{Ky} + Be^{-Ky} \tag{A-26}$$

Substituting Eq. (A-26) into Eq. (A-24) and solving for $\hat{v}$ yields

$$\hat{v} = \left[\frac{2AKy + 4CK^2 - A}{4K^2}\right]e^{Ky} - \left[\frac{2BKy - 4DK^2 + B}{4K^2}\right]e^{-Ky}. \tag{A-27}$$

[where A, B, C, and D are arbitrary constants to be determined by the boundary conditions Eqs. (A-14), (A-15), and (A-22)]. Application of Eq. (A-22) results in the following:

$$C - \frac{A}{4K^2} + D - \frac{B}{4K^2} = 0 \tag{A-28}$$

The constraints on $\hat{v}$ and its y-derivative at $y = \infty$ produce

$$\hat{v}(\infty) = \lim_{y\to\infty}\left[\frac{2AKy + 4CK^2 - A}{4K^2}\, e^{Ky}\right] \tag{A-29}$$

$$\hat{v}'(\infty) = \lim_{y\to\infty}\left[\frac{-A + 2KAy + 4CK^2}{4K}\, e^{Ky}\right] \tag{A-30}$$

Equations (A-14) and (A-15) imply $A = C = 0$. Substituting Eq. (A-27) into (A-23) yields

$$\hat{v}'(0) = \frac{-A + 4CK^2}{4K} - \frac{B + 4DK^2}{4K} = i\alpha\hat{\eta}\sigma \tag{A-31}$$

Using $A = C = 0$, and Eqs. (A-28) and (A-31), the constants B and D can be solved for:

$$B = -2i\alpha\hat{\eta}\sigma K;\ D = -i\alpha\hat{\eta}\sigma/2K \tag{A-32}$$

Therefore the expression for $\hat{v}$ that satisfies the boundary conditions is

$$\hat{v}(y) = i\alpha\hat{\eta}\sigma y\, e^{-Ky} \tag{A-33}$$

Using similar techniques, the functions $\hat{u}$ and $\hat{w}$ may be determined; the results are summarized as follows:

$$\hat{u}(y) = \frac{\alpha^2\hat{\eta}\sigma}{K}\, ye^{-Ky} - \sigma\hat{\eta}e^{-Ky} = \left[\frac{\alpha^2}{K}\, y - 1\right]\sigma\hat{\eta}e^{-Ky} \tag{A-34}$$

$$\hat{w}(y) = \left(\frac{\alpha K}{\beta} - \frac{\alpha^3}{BK}\right)\hat{\eta}\sigma y e^{-Ky} \tag{A-35}$$

Final Solution for Velocity, Pressure and Shear Stress. Using the solutions reported in Eqs. (A-33) through (A-35), the final form of the velocities and pressure can be written as the real part of Eqs. (A-7) through (A-10):

$$u = \left[\frac{\alpha}{K}\, y - 1\right]\hat{\eta}\sigma e^{-Ky}\cos(\alpha x + \beta z) + \sigma y \tag{A-36}$$

$$v = -\alpha\hat{\eta}\sigma y e^{-Ky}\sin(\alpha x + \beta z) \tag{A-37}$$

$$w = \frac{\beta\alpha\hat{\eta}\sigma}{K}\, ye^{-Ky}\sin(\alpha x + \beta z) \tag{A-38}$$

$$P = -2\mu\alpha\hat{\eta}\sigma e^{-Ky}\sin(\alpha x + \beta z) \tag{A-39}$$

The shear stress imposed by the fluid on the wavy surface may be calculated with the following formula

$$\tau_{yx} = \mu\left(\frac{\partial u}{\partial y} + \frac{\partial v}{\partial x}\right) \tag{A-40}$$

$$\tau_{yz} = \mu\left(\frac{\partial v}{\partial z} + \frac{\partial w}{\partial y}\right) \tag{A-41}$$

Their values are given below:

$$\tau_{yx} = \mu\sigma\left[\frac{\alpha^2 + K^2}{K}\,\hat{\eta} - 2\alpha^2\hat{\eta}y\right]e^{-Ky}\cos(\alpha x + \beta z) + \mu\sigma \tag{A-42}$$

$$\tau_{yz} = \mu\sigma\left[\frac{\beta\alpha\hat{\eta}}{K} - 2\beta\alpha\hat{\eta}y\right]e^{-Ky}\cos(\alpha x + \beta z) \tag{A-43}$$

At the cell surface ($y = 0$ in the linearized solution), the shear stresses are

$$\tau_{yx}|_{y=0} = \mu\sigma + \frac{\mu\sigma(\alpha^2 + K^2)\hat{\eta}}{K}\cos(\alpha x + \beta z) \tag{A-44}$$

$$\tau_{yz}|_{y=0} = \mu\sigma\,\frac{\beta\alpha\hat{\eta}}{K}\cos(\alpha x + \beta z) \tag{A-45}$$